Compact Adiabatic Polarization Splitter-Rotator on Thin-Film Lithium Niobate

Yinan Wu, Xuerui Sun, Xiaotian Xue, Hao Li, Shijie Liu, Yuanlin Zheng, and Xianfeng Chen

***Abstract*—Polarization controlling devices on thin-film lithium niobate (TFLN) are critical components for photonic integrated circuits (PICs) on the platform because the birefringence of lithium niobate intrinsically determines its polarization-dependent property. Here, we propose and demonstrate a compact polarization splitter-rotator (PSR) on TFLN based on two adiabatic tapers and an asymmetric directional coupler with an effective length of only 240 μm. The device is fabricated via a one-step electron beam lithography (EBL) and inductively coupled plasma (ICP) etching process. Our device shows efficient polarization extinction at the telecom C-band, providing a polarization extinction ratio (PER) of 26.6 dB and 12.2 dB for TE and TM mode, respectively. The highest PER both exceed 30 dB at 1544 nm and the insertion loss both less than 0.91 dB. The device is expected to apply to efficient polarization multiplexing and polarization modulating, an indispensable component of the PICs on TFLN in the future.**

***Index Terms*—Adiabatic coupling, polarization splitter-rotator, thin-film lithium niobate.**

I. Introduction

As an emerging multifunctional optical material, thin-film lithium niobate (TFLN) is considered as one of the most promising photonic integration platforms [1], [2], [3], [4], [5], [6], [7], [8], [9], [10]. TFLN retains the excellent optical properties of crystalline lithium niobate (LN), such as high refractive index, wide transmission spectrum, large nonlinear and electro-optic coefficients. Light can be well confined and manipulated in TFLN micro-/nano-waveguides by leveraging the high refractive index contrast between LN and silica. Taking advantage of the superior optical properties of LN, a large number of integrated devices with excellent performance have been demonstrated on the TFLN platform [11], [12], [13], [14], [15], [16], [17], [18], [19], [20]. In recent years, varieties of electro-optic modulators [11], [17], [21], [22], [23], [24], [25], [26], nonlinear frequency conversion [12], [14], [15], [16], [19], [27], parametric oscillation [28], [29], optical frequency combs [21], [30], [31], [32], and quantum light sources [13], [33] based on TFLN have been reported. With the rapid development of TFLN integration technology, independent devices with different functions will be integrated on the same chip on a large scale in the short future. Therefore, the basic device units such as polarization controlling [34], [35], [36], [37], wavelength division multiplexing [38], [39], and multimode interference coupler [40] are becoming more and more critical.

The birefringence effect of LN intrinsically determines its anisotropic property. Light propagating in different directions experiences different refractive indices, which makes the high-performance polarization controlling device on TFLN urgently demanded. For instance, in order to utilize the largest coefficient for nonlinear or electro-optic effects on TFLN, a specific polarization mode is required. Compared with polarization beam splitters (PBS) [35], PSRs are more commonly used for polarization management. This kind of polarization controlling device is a necessary part of the mode division multiplexing system [41], [42] and polarization multiplexing system [42], [43]. Therefore, the study of high-performance PSR devices has high practical value and great application potential. Various efficient PSRs have been demonstrated on silicon platform [44], [45], [46], [47], [48], [49]. These devices can be divided into two types: coupling-type and evolution-type. For coupling-type PSRs, the core structure is a directional coupler (DC). According to the cross-polarization coupling principle [50], the TM and TE mode can directly couple with each other through the ridge waveguide. This type of PSRs have compact footprint but they are demanding for TFLN platform. For example, PSRs based on subwavelength grating waveguides (SWGs) [46], [47] on TFLN are difficult to realize at present because of the fabrication limitation. PSRs based on bent DC [48], [49] is also rejected by the material's anisotropy. In addition, cross-polarization coupling DCs have the disadvantage of narrow operating bandwidth and high fabricating precision requirement. On the other hand, the

Manuscript received 29 August 2023; revised 23 October 2023 and 21 November 2023; accepted 28 November 2023. Date of publication 1 December 2023; date of current version 2 April 2024. The work was supported in part by the National Natural Science Foundation of China under Grants 12074252, 62022058, 62005159, and 11734011, in part by the National Key Research and Development Program of China under Grant 2018YFA0306301, in part by Shanghai Municipal Science and Technology Major Project under Grant 2019SHZDZX01-ZX06, and in part by Yangyang Development Fund. *(Corresponding authors: Yuanlin Zheng; Xianfeng Chen.)*

Yinan Wu, Xuerui Sun, Xiaotian Xue, Hao Li, and Shijie Liu are with the State Key Laboratory of Advanced Optical Communication Systems and Networks, School of Physics and Astronomy, Shanghai Jiao Tong University, Shanghai 200240, China (e-mail: wyn_cn@sjtu.edu.cn; sxr0306@sjtu.edu.cn; xue_xiaotian@sjtu.edu.cn; lihaosky@sjtu.edu.cn; 282017047@qq.com).

Yuanlin Zheng is with the State Key Laboratory of Advanced Optical Communication Systems and Networks, School of Physics and Astronomy, Shanghai Jiao Tong University, Shanghai 200240, China, and also with the Shanghai Research Center for Quantum Sciences, Shanghai 201315, China (e-mail: ylzheng@sjtu.edu.cn).

Xianfeng Chen is with the State Key Laboratory of Advanced Optical Communication Systems and Networks, School of Physics and Astronomy, Shanghai Jiao Tong University, Shanghai 200240, China, also with the Shanghai Research Center for Quantum Sciences, Shanghai 201315, China, and also with the Collaborative Innovation Center of Light Manipulations and Applications, Shandong Normal University, Jinan 250358, China (e-mail: xfchen@sjtu.edu.cn).

Color versions of one or more figures in this article are available at https://doi.org/10.1109/JLT.2023.3338229.

Digital Object Identifier 10.1109/JLT.2023.3338229

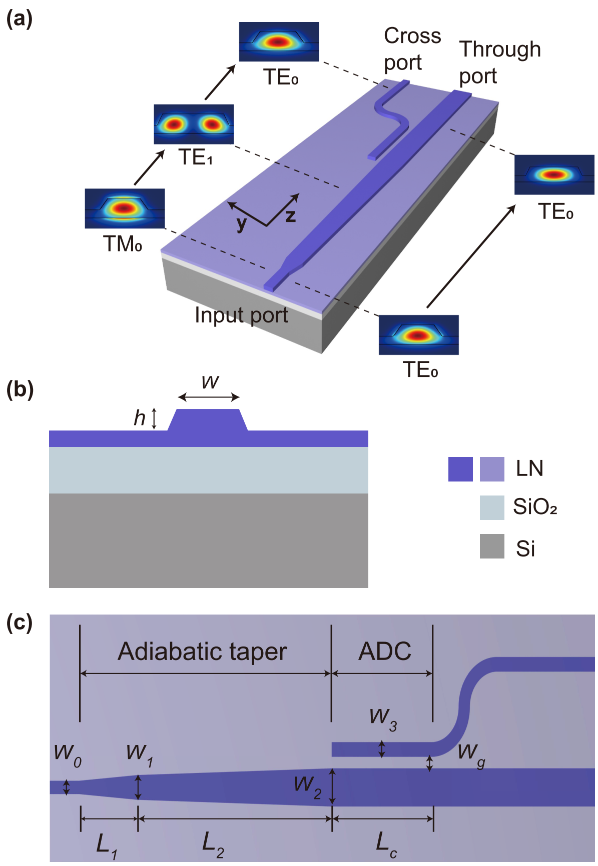

Fig. 1. (a) Schematic illustration of the PSR on TFLN. (b) Cross section and (c) top view of the PSR (not to scale).

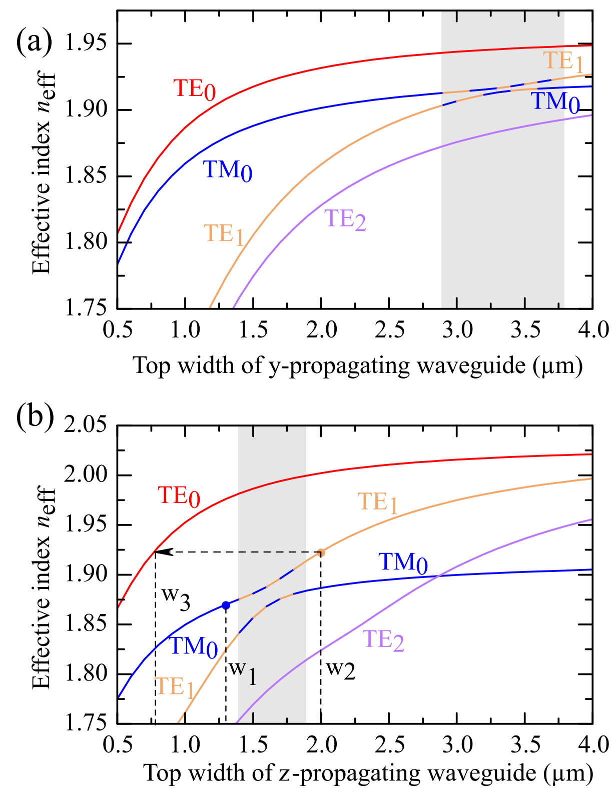

Fig. 2. Effective refractive indices for the lowest order modes at the wavelength of 1550 nm with respect to the waveguide width when the waveguide is aligned along (a) *y*-axis and (b) *z*-axis of TFLN.

evolution-type PSR, which is composed of adiabatic taper and DC with the same polarization coupling, has these disadvantages mitigated. This type of PSR is also more suitable for the TFLN platform due to its simple fabrication and large tolerance. So far, a few evolution-type PSRs on TFLN have been reported [36], [51], [52], [53], [54], but the lengths of these devices are long, some even reaching the millimeter level, which is not favorable in dense integration.

Here, we demonstrated a compact PSR on TFLN based on two adiabatic tapers and an asymmetric DC. The device is fabricated via a one-step electron beam lithography (EBL) and inductively coupled plasma (ICP) etching process. The total length of the device is only 240 μm, and the TE and TM polarization modes have high extinction ratios within the entire telecom-C band. The experimentally measured polarization extinction ratios (PERs) of TE and TM modes exceed 26.6 dB and 10.6 dB respectively in the wavelength range of 1520-1570 nm. At the same time, the PER of the two orthogonal modes both exceed 30 dB at the wavelength of 1544 nm.

II. Device Design and Numerical Simulation

Fig. 1(a) depicts the schematic of the PSR on the 600-nm-thick x-cut TFLN platform. The TFLN is bonded on top of a 2-μm-thick SiO_2 buffering layer and a 500-μ m-thick Si substrate. The PSR device consists of an adiabatic taper and an asymmetric directional coupler (ADC). The TE_0 mode propagates directly to the through port without mode conversion and mode coupling. For TM_0 input, the TM_0 mode can be converted into the TE_1 mode efficiently in the adiabatic taper. Then the TE_1 mode is coupled to the cross port through the ADC and simultaneously converted into TE_0 mode. As shown in Fig. 1(b), the TFLN waveguide is usually a half-etched ridge waveguide which is asymmetric along the vertical direction due to the etching condition. The TM_0 and TE_1 modes experience mode hybridization within a certain waveguide width range. In the numerical simulation, the etching depth h of the waveguide is set to be 350 nm to ensure the existence of TM modes. The etching angle is 63°, according to the actual etching condition. Fig. 1(c) shows that the adiabatic taper is divided into two segments and the typical width and length parameters of the taper is denoted as w_0, w_1, w_2, L_1, and L_2, respectively. The coupling length and coupling gap of the ADC are denoted as L_c and w_g.

Fig. 2 illustrates the calculated effective refractive indices, n_{eff}, of the four lowest-order eigenmodes at 1550 nm varying with the top width, w, of the ridge waveguide along the y-axis and z-axis, respectively. There exists the condition for mode hybridization between the TM_0 and TE_1 mode when w is near 3.3 μm and 1.6 μm for the y-propagating and z-propagating waveguide, respectively, as marked by the grey area. For the y-propagating waveguide, the top width w corresponding to mode hybridization is much wider than that of the single mode

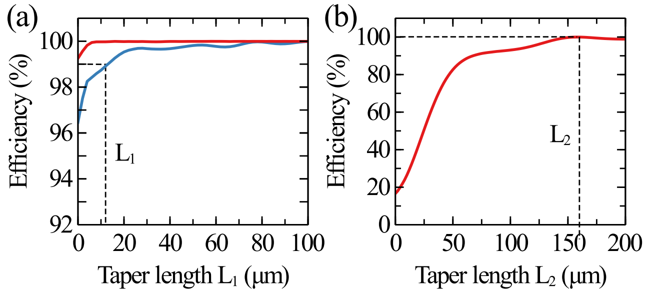

Fig. 3. (a) Transmittance of TE_0 and TM_0 mode in the first taper versus the taper length L_1. (b) Conversion efficiency from TM_0 to TE_1 mode in the second taper versus the taper length L_2.

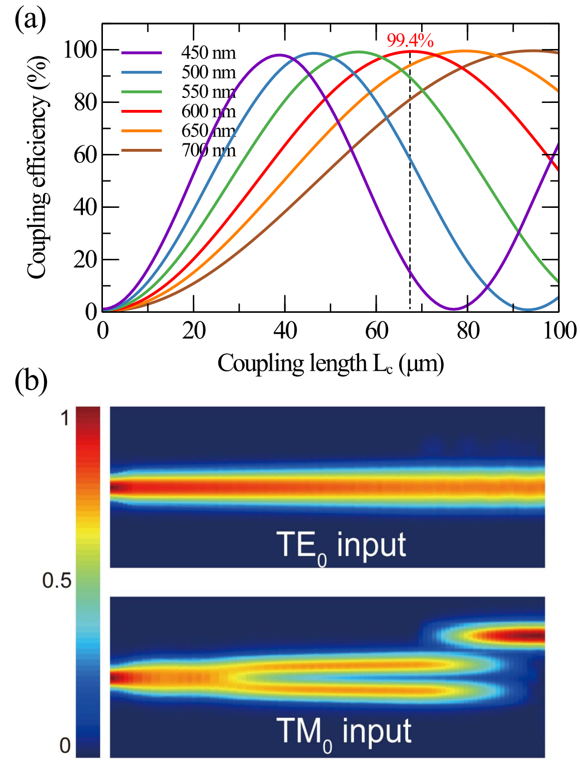

Fig. 4. (a) Coupling efficiencies from TE_1 to TE_0 mode in ADC versus the directional coupling length L_c at different coupling gaps w_g. (b) Light propagation in the PSR at 1550 nm.

condition. Thus, the adiabatic taper needs to be very long even to the order of millimeters in order to achieve efficient conversion from TM_0 to TE_1 mode and low transition loss of TM_0 mode from single-mode waveguide to the wide waveguide. The TFLN waveguide is usually set along the y-direction in electro-optic or nonlinear applications, resulting in that the length of the device is too long to meet the miniaturization requirement of the PICs. In our design, the PSR is aligned along the z-axis. In this way, the mode conversion from TM_0 to TE_1 mode (the mode hybridization region) happens when the taper width is approximately 1.4–1.9 μm, see also Fig. 2(b). The top width of the whole adiabatic taper w_0, w_1 and w_2 need to satisfy $w_0 < w_1 < 1.4$ μm < 1.9 μm $< w_2$. Firstly, the input waveguide needs to support only fundamental TE and TM mode. According to Fig. 2(b), the single-mode condition is satisfied when $w < 0.8\,\mu$m. In our configuration, we choose $w_0 = 0.7\,\mu$m. The width of the other segment is set to vary from 1.3 μm to 2 μm to ensure efficient mode conversion from TM_0 to TE_1 mode. Under this condition, there is no mode hybridization with the TE_0 mode.

Next, the taper lengths of L_1 and L_2 need to be optimized to achieve maximum mode conversion efficiency. The length of the first segment is relatively short because the function of this part is to make the fundamental mode in the input waveguide smoothly transit to the hybridization waveguide and the width difference between w_0 and w_1 is small. Fig. 3(a) shows the fundamental mode transmittance of the L_1 segment as a function of its length for the TM_0 and TE_0 mode. The transmittance of both TM_0 and TE_0 mode exceeds 99% when L_1 is longer than 12 μm. The length L_2 of the second segment is optimized under the condition of $L_1 = 12$ μm. The conversion efficiency from TM_0 mode to TE_1 mode is higher than 99.9% when L_2 is set to 160 μm, as shown in Fig. 3(b). The TM_0 mode in the input waveguide is almost completely converted to the TE1 mode by the 172-μm long adiabatic taper while the propagation of the TE_0 mode is unaffected.

Then, an ADC is designed to separate the TE_1 and TE_0 modes. According to Fig. 2(a), the n_{eff} of TE_1 mode is 1.923 while $w_2 = 2\,\mu$m. Consequently, the width of the output waveguide to the cross port, w_3, is set to be 0.77 μm to meet the phase-matching condition of the ADC and the width exactly satisfies the single-mode condition, as marked by the horizontal dotted arrow. Under the same condition, no mode in the output waveguide matches the TE_0 mode in the taper waveguide. So, the TE_0 mode will propagate straight forward along the waveguide to the through port without mode coupling. The coupling length L_c and the waveguide gap w_g are optimized according to the width w_3 of the output waveguide. Fig. 4(a) shows the coupling efficiency varying with the length L_c of the ADC with different coupling gaps at 1550 nm. The gap w_g is chosen to be 600 nm in our design, considering the fabrication precision as well as to reduce the length of the device as much as possible. The calculated coupling length is 68 μm with a conversion efficiency of 99.4%. Finally, an S-bend waveguide is placed at the end of the cross port to separate the two ports. Empirically, a size of 20×100 μm^2 for the S-bend waveguide is good enough for light propagating with little loss. For the though port, we directly use the wide waveguide in the ADC as the output waveguide because only few TE_1 mode remains in the through port and there are no other higher-order modes theoretically. Fig. 4(b) shows the simulated light propagation along the PSR device when inputting the TE_0 and TM_0 mode, respectively, at the wavelength of 1550 nm.

Then, the broadband performance of the PSR device is investigated. Fig. 5 shows the calculated transmission spectra for TM_0, TE_0 and TE_1 modes at the two output ports over the bandwidth of 1500–1600 nm for the TE_0 and TM_0 mode input, respectively. The transmittance to the through port is nearly unity and the polarization extinction ratio (PER) is maintained high (above 30 dB) within the whole band for the TE_0 mode input, as

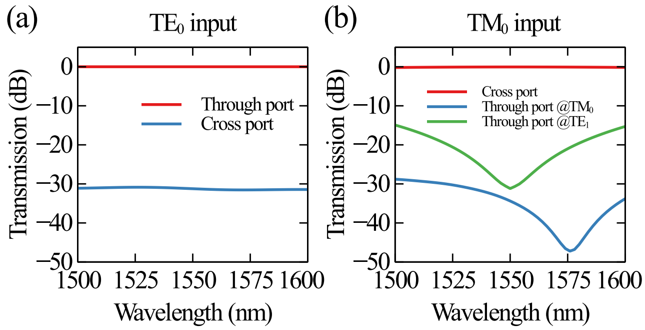

Fig. 5. Simulated transmission spectra at the through and cross ports for (a) TE_0 and (b) TM_0 mode input.

TE_0 mode does not experience mode hybridization throughout the entire device. For TM_0 mode input, the transmittance to the cross port is close unity within the whole band. While at the through port, although the TM_0 mode has been suppressed below −28.8 dB, there is still a small portion of TE_1 mode existing. The TM_0 and TE_1 modes in through port show different transmission spectrum because the residual TM_0 mode comes from the ADC while the TE_1 mode comes from the ADC. Therefore, unlike the TE mode input, the PER of the TM mode input has a moderate wavelength sensitivity due to the characteristics of the ADC. Still, the PER exceeds 18.7 dB for a wide wavelength range spanning from 1520 to 1570 nm and the maximum PER is very close to 30 dB at 1550 nm. The designed PSR has a high extinction performance over a wide bandwidth.

Finally, the tolerance of the device is considered. For the PSR device, the ADC has a higher requirement for fabrication accuracy than the adiabatic taper. It is worth mentioning that the phase matching condition can be well satisfied in the ADC, because the slope difference of the curves of TE_0 and TE_1 mode is very small, see also Fig. 2(a), and the simultaneous increase or decrease of w_2 and w_3 only causes a slight drift of the central wavelength. The tolerance of the PSR is investigated by introducing ±10 nm and ±20 nm discrepancy to the coupling gap w_g. As shown in Fig. 6, the central wavelength has a blue shift when w_g gets wider. The PER of TM mode is more sensitive to the variation because the TM mode has undergone once mode conversion and once directional coupling. However, the operating bandwidth of the device is not greatly affected. The PER of TE and TM modes is still higher than 29 dB and 14 dB, respectively, over the wavelength spanning from 1520-1570 nm. This means that the PSR has a large fabrication tolerance considering the precision during the lithography and etching process.

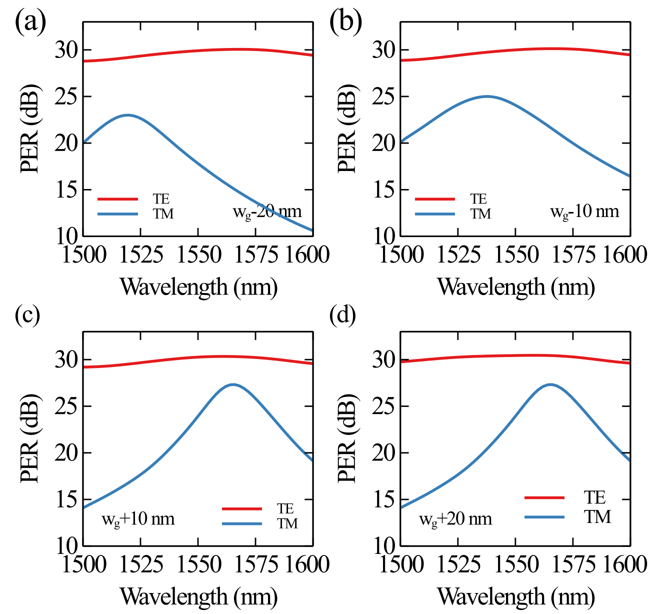

Fig. 6. PER of TE and TM modes with different width deviation in the designed ADC. (a) −20 nm (b) −10 nm (c) +10 nm (d) +20 nm in the designed ADC.

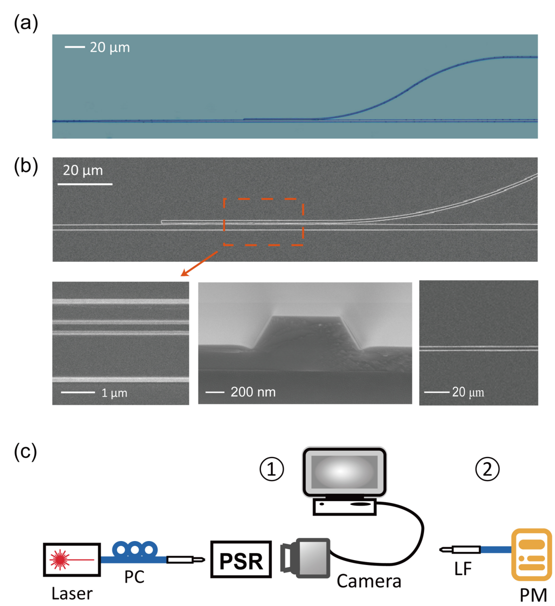

Fig. 7. (a) Optical microscope and (b) SEM images of the fabricated PSR, the cross section of the input waveguide and a straight waveguide. (c) The characterization experimental setup. PC, polarization controller; LF, lensed fiber; PM, powermeter.

III. Device Fabrication and Characterization

The PSR device is fabricated using a commercial x-cut TFLN wafer (NANOLN) consisting of a 600-nm thick LN layer, a 2-μm silica layer, and a 500-μm silicon substrate. The preparation process of the device is divided into three major parts. Firstly, a 665-nm thick amorphous silicon is deposited as a hard etching mask by plasma-enhanced chemical vapor deposition (PECVD). Next, a layer of resist is spin-coated on the surface of amorphous silicon and exposed by electron beam lithography (EBL). The pattern is transferred to the silicon mask layer and the TFLN with the inductively coupled plasma (ICP) etching. The residual silicon mask is removed by KOH solution. Finally, the chip is diced and the facets are polished for lensed fiber coupling. The sample is fabricated at the Center for Advanced Electronic Materials and Devices, SJTU.

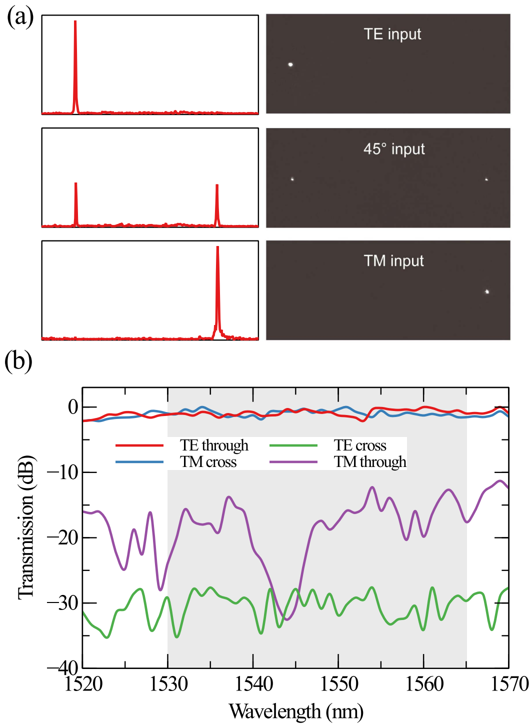

Fig. 8. (a) Output intensity distribution and mode profiles at different input polarization states, i.e., TE, 45°, TM mode input. (b) Experimental transmission at through and cross ports for TE and TM mode input.

Fig. 7(a) shows the optical microscope image of the fabricated PSR device. The total length of the PSR is only 240 μm, significantly shorter than previous reports [36], [51], [52], [53], [54]. Fig. 7(b) shows the scanning electron microscopy (SEM) images and the enlarged view of the ADC, the cross section of the input waveguide and straight waveguide, as marked in the dashed zone. The widths of the two coupled waveguide of the ADC are 0.78 μm and 2 μm, with a coupling gap of 0.62 μm. The waveguide width, etching depth and sidewall angle is measured to be 718 nm, 350 nm and 61.3°, respectively, which is consistent with our designed parameters. In addition, a single straight waveguide is made for the coupling loss measurement. Fig. 7(c) shows the experimental setup for the device characterization. Light source provided by a tunable laser source passes through a polarization controller (PC) and is coupled into the PSR through a lensed fiber (LF). Light from the output ports is imaged using an infrared camera for mode profiling or collected using another lensed fiber for power measurement.

Fig. 8(a) displays the intensity distribution and the mode profiles of the output channels with different polarization states input. The PSR device realizes great polarization extinction performance. For quantitatively characterization, the maximum and minimum power values of the through and cross ports are respectively measured by adjusting the PC and the PER of the PSR is determined. The device insertion loss is determined by measuring the power of a straight waveguide to normalize the output power. In our experiment, the on-chip insertion loss of the PSR for TE and TM mode input is approximately 0.91 dB and 0.38 dB at 1550 nm, respectively. Fig. 8(b) shows the measured normalized transmittance of the two ports for TE and TM polarized input. The experimental results are well consistent with the theoretical prediction. The measured PER for TE and TM mode input exceeds 26.6 dB and 10.6 dB over 1520-1570 nm, respectively. And the PER for TM mode is greater than 12.2 dB covering the telecom C-band. The maximum PERs of TE and TM both exceed 30 dB at 1544 nm, only a small deviation away from the simulation result.

TABLE I
COMPARISON OF PSR PERFORMANCE ON TFLN

Ref.	Length/μm	PER/dB	IL/dB	Bandwidth/nm
[36]	431	>20	0.65	80 (1275–1355)
[37]	440	>26.6 TE >19.6 TM	1	60 (1520–1580)
[51]	>1200	>20	1.5	35 (1530–1565)
[52]	8000	~8 TE ~10 TM	2 TE 3 TM	130 (1500–1630)
[53]	679	>20 TE >10 TM	1.5	47 (1502–1649)
[54]	405	>22 TE >11 TM	2	160 (1480–1640)
This work	240	>26.6 TE >10.6 TM	0.91 TE 0.38 TM	50 (1520–1570)

Table I summarizes recent progress of PSR on TFLN. Among all the following devices, our PSR shows the shortest length and the insertion loss is competitive with other studies. Meanwhile, the PER of our devices is at a good level. It is worth mentioning that our device possesses the highest PER of over 30 dB for both TE and TM polarization within the central wavelength range. Although compared with works in Refs. [52], [54], our PSR have a relatively narrower bandwidth, the high bandwidth performance is obtained by sacrificing the effective length and insertion loss.

The results confirm the high performance of our PSR design in the telecom C-band thanks to its double adiabatic feature. The device is readily applicable for efficient polarization multiplexing and polarization modulating, which will become an indispensable component of the PICs on TFLN in the future.

IV. Conclusion

In conclusion, we have demonstrated a compact PSR on TFLN with an effective length of only 240 μm, which is the shortest length compared with the current similar work. The fabricated PSR exhibits a high-performance PER of over 26.6 dB and 12.2 dB for TE and TM mode, respectively, over the whole telecom-C band and the highest PER simultaneously exceeds 30 dB at the central wavelength. Moreover, the device has a simple structure and only needs a single-step EBL and ICP process with a large fabrication tolerance. Therefore, the device is expected to apply to efficient polarization multiplexing and polarization modulating, which will become an indispensable component of the photonic integrated circuits on TFLN in the future.

References

[1] A. Boes et al., "Lithium niobate photonics: Unlocking the electromagnetic spectrum," *Science*, vol. 379, no. 6627, 2023, Art. no. eabj4396, doi: 10.1126/science.abj4396.

[2] A. Boes, B. Corcoran, L. Chang, J. Bowers, and A. Mitchell, "Status and potential of lithium niobate on insulator (LNOI) for photonic integrated circuits," *Laser Photon. Rev.*, vol. 12, no. 4, 2018, Art. no. 1700256, doi: 10.1002/lpor.201700256.

[3] J. Lin, F. Bo, Y. Cheng, and J. Xu, "Advances in on-chip photonic devices based on lithium niobate on insulator," *Photon. Res.*, vol. 8, no. 12, pp. 1910–1936, Dec. 2020. [Online]. Available: http://opg.optica.org/prj/abstract.cfm?URI=prj-8-12-1910

[4] A. Honardoost, K. E. A. Abdelsalam, and S. Fathpour, "Rejuvenating a versatile photonic material: Thin–film lithium niobate," *Laser Photon. Rev.*, vol. 14, 2020, Art. no. 2000088, doi: 10.1002/lpor.202000088.

[5] Y. Qi and Y. Li, "Integrated lithium niobate photonics," *Nanophotonics*, vol. 9, no. 6, pp. 1287–1320, 2020, doi: 10.1515/nanoph-2020-0013.

[6] Y. Zheng and X. Chen, "Nonlinear wave mixing in lithium niobate thin film," *Adv. Phys.: X*, vol. 6, no. 1, 2021, Art. no. 1889402, doi: 10.1080/23746149.2021.1889402.

[7] D. Zhu et al., "Integrated photonics on thin-film lithium niobate," *Adv. Opt. Photon.*, vol. 13, no. 2, pp. 242–352, Jun. 2021. [Online]. Available: https://opg.optica.org/aop/abstract.cfm?URI=aop-13-2-242

[8] S. Saravi, T. Pertsch, and F. Setzpfandt, "Lithium niobate on insulator: An emerging platform for integrated quantum photonics," *Adv. Opt. Mater.*, vol. 9, no. 22, 2021, Art. no. 2100789. [Online]. Available: https://onlinelibrary.wiley.com/doi/abs/10.1002/adom.202100789

[9] Y. Jia, L. Wang, and F. Chen, "Ion-cut lithium niobate on insulator technology: Recent advances and perspectives," *Appl. Phys. Rev.*, vol. 8, Feb. 2021, Art. no. 011307, doi: 10.1063/5.0037771.

[10] A. Honardoost, K. Abdelsalam, and S. Fathpour, "Rejuvenating a versatile photonic material: Thin-film lithium niobate," *Laser Photon. Rev.*, vol. 14, no. 9, 2020, Art. no. 2000088, doi: 10.1002/lpor.202000088.

[11] C. Wang et al., "Integrated lithium niobate electro-optic modulators operating at CMOS-compatible voltages," *Nature*, vol. 562, no. 7725, pp. 101–104, Oct. 2018, doi: 10.1038/s41586-018-0551-y.

[12] C. Wang et al., "Ultrahigh-efficiency wavelength conversion in nanophotonic periodically poled lithium niobate waveguides," *Optica*, vol. 5, no. 11, pp. 1438–1441, Nov. 2018. [Online]. Available: https://opg.optica.org/optica/abstract.cfm?URI=optica-5-11-1438

[13] J. Zhao et al., "Shallow-etched thin-film lithium niobate waveguides for highly-efficient second-harmonic generation," *Opt. Exp.*, vol. 28, no. 13, pp. 19669–19682, Jun. 2020. [Online]. Available: https://opg.optica.org/oe/abstract.cfm?URI=oe-28-13-19669

[14] J. Lu et al., "Periodically poled thin-film lithium niobate microring resonators with a second-harmonic generation efficiency of 250,000%/W," *Optica*, vol. 6, no. 12, pp. 1455–1460, Dec. 2019. [Online]. Available: https://opg.optica.org/optica/abstract.cfm?URI=optica-6-12-1455

[15] S. Liu, Y. Zheng, Z. Fang, X. Ye, Y. Cheng, and X. Chen, "Effective four-wave mixing in the lithium niobate on insulator microdisk by cascading quadratic processes," *Opt. Lett.*, vol. 44, no. 6, pp. 1456–1459, Mar. 2019. [Online]. Available: https://opg.optica.org/ol/abstract.cfm?URI=ol-44-6-1456

[16] X. Ye, S. Liu, Y. Chen, Y. Zheng, and X. Chen, "Sum-frequency generation in lithium-niobate-on-insulator microdisk via modal phase matching," *Opt. Lett.*, vol. 45, no. 2, pp. 523–526, Jan. 2020. [Online]. Available: https://opg.optica.org/ol/abstract.cfm?URI=ol-45-2-523

[17] Y. He et al., "Self-starting bi-chromatic $LiNbO_3$ soliton microcomb," *Optica*, vol. 6, no. 9, pp. 1138–1144, Sep. 2019. [Online]. Available: https://opg.optica.org/optica/abstract.cfm?URI=optica-6-9-1138

[18] M. Yu, B. Desiatov, Y. Okawachi, A. L. Gaeta, and M. Lončar, "Coherent two-octave-spanning supercontinuum generation in lithium-niobate waveguides," *Opt. Lett.*, vol. 44, no. 5, pp. 1222–1225, Mar. 2019. [Online]. Available: https://opg.optica.org/ol/abstract.cfm?URI=ol-44-5-1222

[19] J. Zhao, C. Ma, M. Rüsing, and S. Mookherjea, "High quality entangled photon pair generation in periodically poled thin-film lithium niobate waveguides," *Phys. Rev. Lett.*, vol. 124, Apr. 2020, Art. no. 163603, doi: 10.1103/PhysRevLett.124.163603.

[20] Y. Liang et al., "A high-gain cladded waveguide amplifier on erbium doped thin-film lithium niobate fabricated using photolithography assisted chemo-mechanical etching," *Nanophotonics*, vol. 11, no. 5, pp. 1033–1040, 2022, doi: 10.1515/nanoph-2021-0737.

[21] M. He et al., "High-performance hybrid silicon and lithium niobate Mach–Zehnder modulators for 100 gbits-1 and beyond," *Nature Photon.*, vol. 13, no. 5, pp. 359–364, May 2019, doi: 10.1038/s41566-019-0378-6.

[22] X. Sun et al., "Experimental investigation on the unbalanced Mach–Zehnder interferometer on lithium niobate thin film," *Chin. Opt. Lett.*, vol. 20, no. 10, Oct. 2022, Art. no. 101301. [Online]. Available: https://opg.optica.org/col/abstract.cfm?URI=col-20-10-101301

[23] X. Liu et al., "Broadband meandered thin-film lithium niobate modulator with ultra-low half-wave voltage," *IEEE Photon. Technol. Lett.*, vol. 34, no. 8, pp. 424–427, Apr. 2022.

[24] J. Cai, C. Guo, C. Lu, A. P. T. Lau, P. Chen, and L. Liu, "Design optimization of silicon and lithium niobate hybrid integrated traveling-wave Mach-Zehnder modulator," *IEEE Photon. J.*, vol. 13, no. 4, pp. 1–6, Aug. 2021.

[25] L. Yu et al., "Design of high-speed mid-infrared electro-optic modulator based on thin film lithium niobate," *IEEE Photon. J.*, vol. 14, no. 2, Apr. 2022, Art. no. 6621506.

[26] C. Damgaard-Carstensen and S. I. Bozhevolnyi, "Nonlocal electro-optic metasurfaces for free-space light modulation," *Nanophotonics*, vol. 12, no. 14, pp. 2953–2962, 2023, doi: 10.1515/nanoph-2023-0042.

[27] Y. Zhang et al., "Scalable, fiber-compatible lithium-niobate-on-insulator micro-waveguides for efficient nonlinear photonics," *Optica*, vol. 10, no. 6, pp. 688–693, Jun. 2023. [Online]. Available: https://opg.optica.org/optica/abstract.cfm?URI=optica-10-6-688

[28] J. Lu, A. A. Sayem, Z. Gong, J. B. Surya, C.-L. Zou, and H. X. Tang, "Ultralow-threshold thin-film lithium niobate optical parametric oscillator," *Optica*, vol. 8, no. 4, pp. 539–544, Apr. 2021. [Online]. Available: https://opg.optica.org/optica/abstract.cfm?URI=optica-8-4-539

[29] M. Jankowski et al., "Ultrabroadband nonlinear optics in nanophotonic periodically poled lithium niobate waveguides," *Optica*, vol. 7, no. 1, pp. 40–46, Jan. 2020. [Online]. Available: http://opg.optica.org/optica/abstract.cfm?URI=optica-7-1-40

[30] M. Zhang et al., "Broadband electro-optic frequency comb generation in a lithium niobate microring resonator," *Nature*, vol. 568, no. 7752, pp. 373–377, Apr. 2019, doi: 10.1038/s41586-019-1008-7.

[31] M. Xu, M. He, Y. Zhu, S. Yu, and X. Cai, "Flat optical frequency comb generator based on integrated lithium niobate modulators," *J. Lightw. Technol.*, vol. 40, no. 2, pp. 339–345, Jan. 2022.

[32] Y. Okawachi et al., "Chip-based self-referencing using integrated lithium niobate waveguides," *Optica*, vol. 7, no. 6, pp. 702–707, Jun. 2020. [Online]. Available: https://opg.optica.org/optica/abstract.cfm?URI=optica-7-6-702

[33] U. A. Javid, J. Ling, J. Staffa, M. Li, Y. He, and Q. Lin, "Ultrabroadband entangled photons on a nanophotonic chip," *Phys. Rev. Lett.*, vol. 127, Oct. 2021, Art. no. 183601, doi: 10.1103/PhysRevLett.127.183601.

[34] X. Sun et al., "Thin-film lithium niobate polarization modulator without polarization diversity," *Opt. Exp.*, vol. 30, no. 17, pp. 30592–30599, Aug. 2022. [Online]. Available: https://opg.optica.org/oe/abstract.cfm?URI=oe-30-17-30592

[35] Y. Wu et al., "Lithium niobate thin film polarization beam splitter based on asymmetric directional coupling," *J. Lightw. Technol.*, vol. 40, no. 24, pp. 7843–7847, Dec. 2022. [Online]. Available: https://opg.optica.org/jlt/abstract.cfm?URI=jlt-40-24-7843

[36] H. Luo et al., "High-performance polarization splitter-rotator based on lithium niobate-on-insulator platform," *IEEE Photon. Technol. Lett.*, vol. 33, no. 24, pp. 1423–1426, Dec. 2021.

[37] X. Wang, A. Pan, T. Li, C. Zeng, and J. Xia, "Efficient polarization splitter-rotator on thin-film lithium niobate," *Opt. Exp.*, vol. 29, no. 23, pp. 38044–38052, Nov. 2021. [Online]. Available: https://opg.optica.org/oe/abstract.cfm?URI=oe-29-23-38044

[38] K. Chen et al., "Four-channel CWDM transmitter chip based on thin-film lithium niobate platform," *J. Semicond.*, vol. 43, no. 11, Nov. 2022, Art. no. 112301, doi: 10.1088/1674-4926/43/11/112301.

[39] G. Chen et al., "Four-channel CWDM device on a thin-film lithium niobate platform using an angled multimode interferometer structure," *Photon. Res.*, vol. 10, no. 1, pp. 8–13, Jan. 2022. [Online]. Available: https://opg.optica.org/prj/abstract.cfm?URI=prj-10-1-8

[40] G. Chen, J. D. Ng, H.-L. Lin, G. Zhang, X. Gong, and A. J. Danner, "Design and fabrication of high-performance multimode interferometer in lithium niobate thin film," *Opt. Exp.*, vol. 29, no. 10, pp. 15689–15698, May 2021. [Online]. Available: https://opg.optica.org/oe/abstract.cfm?URI=oe-29-10-15689

[41] Y. Jiang et al., "High-speed optical mode switch in lithium niobate on insulator," *ACS Photon.*, vol. 10, pp. 2257–2263, Jan. 2023, doi: 10.1021/acsphotonics.2c01364.

[42] X. Han et al., "Mode and polarization-division multiplexing based on silicon nitride loaded lithium niobate on insulator platform," *Laser Photon. Rev.*, vol. 16, no. 1, 2022, Art. no. 2100529, doi: 10.1002/lpor.202100529.

[43] Z. Lin et al., "High-performance polarization management devices based on thin-film lithium niobate," *Light: Sci. Appl.*, vol. 11, no. 1, Apr. 2022, Art. no. 93, doi: 10.1038/s41377-022-00779-8.

[44] D. Dai and J. E. Bowers, "Novel concept for ultracompact polarization splitter-rotator based on silicon nanowires," *Opt. Exp.*, vol. 19, no. 11, pp. 10940–10949, May 2011. [Online]. Available: https://opg.optica.org/oe/abstract.cfm?URI=oe-19-11-10940

[45] H. Xu and Y. Shi, "Ultra-broadband silicon polarization splitter-rotator based on the multi-mode waveguide," *Opt. Exp.*, vol. 25, no. 15, pp. 18485–18491, Jul. 2017. [Online]. Available: https://opg.optica.org/oe/abstract.cfm?URI=oe-25-15-18485

[46] Y. Xu and J. Xiao, "Ultracompact and high efficient silicon-based polarization splitter-rotator using a partially-etched subwavelength grating coupler," *Sci. Rep.*, vol. 6, no. 1, Jun. 2016, Art. no. 27949, doi: 10.1038/srep27949.

[47] Y. Wang et al., "Ultra-compact sub-wavelength grating polarization splitter-rotator for silicon-on-insulator platform," *IEEE Photon. J.*, vol. 8, no. 6, Dec. 2016, Art. no. 7805709.

[48] H. Xu and Y. Shi, "Ultra-compact and highly efficient polarization rotator utilizing multi-mode waveguides," *Opt. Lett.*, vol. 42, no. 4, pp. 771–774, Feb. 2017. [Online]. Available: https://opg.optica.org/ol/abstract.cfm?URI=ol-42-4-771

[49] Y. Zhang et al., "Ultra-compact and highly efficient silicon polarization splitter and rotator," *APL Photon.*, vol. 1, no. 9, Oct. 2016, Art. no. 091304, doi: 10.1063/1.4965832.

[50] T. Wang et al., "Cross-polarization generation and its impact on coupler performance," *IEEE J. Sel. Topics Quantum Electron.*, vol. 12, no. 4, pp. 751–759, Jul./Aug. 2006.

[51] L. Song, J. Zhao, X. Dai, M. Lu, Q. Lu, and W. Guo, "Fully adiabatic polarization rotator-splitter based on thin-film lithium niobate platform," *Opt. Exp.*, vol. 31, no. 12, pp. 19604–19612, Jun. 2023. [Online]. Available: https://opg.optica.org/oe/abstract.cfm?URI=oe-31-12-19604

[52] Z. Chen, J. Yang, W.-H. Wong, E. Y.-B. Pun, and C. Wang, "Broadband adiabatic polarization rotator-splitter based on a lithium niobate on insulator platform," *Photon. Res.*, vol. 9, no. 12, pp. 2319–2324, Dec. 2021. [Online]. Available: https://opg.optica.org/prj/abstract.cfm?URI=prj-9-12-2319

[53] C. Deng et al., "Broadband polarization splitter-rotator on lithium niobate-on-insulator platform," *IEEE Photon. Technol. Lett.*, vol. 35, no. 1, pp. 7–10, Jan. 2023.

[54] Y. Shen, Z. Ruan, K. Chen, L. Liu, B. Chen, and Y. Rao, "Broadband polarization splitter-rotator on a thin-film lithium niobate with conversion-enhanced adiabatic tapers," *Opt. Exp.*, vol. 31, no. 2, pp. 1354–1366, Jan. 2023. [Online]. Available: https://opg.optica.org/oe/abstract.cfm?URI=oe-31-2-1354